Ultrafast Heterogeneous Melting of Metals under Extreme Non-equilibrium States

Qiyu Zeng,^{1,2,3} Xiaoxiang Yu,^{1,2,3} Bo Chen,^{1,2,3} Shen Zhang,^{1,2,3} Kaiguo Chen,^{1,2,3} Dongdong Kang,^{1,2,3,*} and Jiayu Dai^{1,2,3,†}

¹College of Science, National University of Defense Technology, 410073 Changsha, Hunan, China

²Hunan Key Laboratory of Extreme Matter and Applications,

National University of Defense Technology, 410073 Changsha, Hunan, China

³Hunan Research Center of the Basic Discipline for Physical States,

National University of Defense Technology, Changsha 410073, China

(Dated: March 3, 2025)

The extreme electron-ion nonequilibrium states created by ultrafast laser excitation challenge conventional melting paradigms. Through neural network-enhanced multiscale simulations of tungsten and gold nanofilms, we identify electronic pressure relaxation as a critical driver of heterogeneous phase transformations. Subpicosecond uniaxial expansion generates density decrease that enable surface-initiated melting far below equilibrium melting temperatures. This ultrafast heterogeneous melting propagates at 2500 m/s—tenfold faster than thermal mechanisms—with characteristic stationary diffraction peak splitting distinguishing it from thermal expansion dynamics. While tungsten shows pressure-driven solid-solid transitions, gold exhibits complete room-temperature amorphization under electronic stress. These results establish hot-electron-mediated lattice destabilization as a universal pathway for laser-induced structural transformations, providing new insights for interpreting time-resolved experiments and controlling laser-matter interactions.

I. INTRODUCTION

Ultrafast laser excitation has emerged as a transformative tool for probing and manipulating matter under extreme nonequilibrium conditions, enabling breakthroughs from attosecond spectroscopy to high-precision nanofabrication [1, 2]. A hallmark of these interactions is the transient electronic excitation that establishes a pronounced temperature disparity between electrons and lattices $(T_e \gg T_i)$ — a nonequilibrium regime where hot electrons coexist with a cold ionic framework. This state, far removed from thermal equilibrium $(T_e = T_i)$, dynamically reconfigures interatomic interactions: charge density redistribution modulates potential energy surfaces (PES), altering bonding forces and energy barriers [3, 4]. Such processes deviate from equilibrium thermodynamic pathways, raising fundamental questions about how materials evolve when energy deposition outpaces thermal relaxation, particularly in laser-induced melting.

The isochoric hypothesis, which assumes negligible volume changes during sub-picosecond heating events, has been the cornerstone of our understanding of material response upon laser excitation. Within this picture, a plethora of femtosecond phenomena have been uncovered: bond hardening [5, 6], phonon softening [7] and dynamic lattice instabilities [8, 9]. These processes occur on timescales of $\sim 10^2$ fs, where inertial stress confinement ensures a quasi-constant density. However, emerging evidence reveals a paradigm shift at picosecond timescales: hot electrons can exert an additional pressure component $p_{\rm e}$ —besides the thermoelastic stress—through thermal

kinetic energy and quantum degeneracy of thermalized electrons [10–12], resulting in a volume change that may challenge the isochoric assumption. In gold, for instance, isobaric calculations predict phonon softening and nonthermal melting [13, 14], in stark contrast with the isochoric hardening evidenced in sub-ps X-ray diffraction experiments [15]. This dichotomy highlights a critical knowledge gap: How does the accumulation of electronic pressure (during $\sim 10^2$ fs) and its relaxation (on $\sim 10^1$ ps timescale) affect structural transformations?

In addressing this issue, the intricacy of the laserdriven process raise challenges. These difficulties arise from the complex interplay among the laser-modulated PES, non-adiabatic electron-ion energy exchange, and microscopic structural transformation processes [9, 16]. Experimentally, the above issues, along with inherent limitations in temporal and spatial resolution, confounds the interpretation of measured data [17–20]. Theoretically, the laser-driven process presents dual requirements that existing methodologies struggle to reconcile: ab initio accuracy to capture the hot-electron-modified PES governing $p_{\rm e}$, and atomic-scale resolution across experimentally relevant thickness (tens of nanometers) to track stress wave propagation and phase transition. This dual requirement significantly constrains the efficacy of existing methodologies, such as classical molecular dynamics combined with two-temperature model [21, 22] or realtime time dependent density functional theory [23, 24], thereby hindering a thorough exploration into the realtime response of laser-excited material without any prior constraints.

Here, we unify *ab initio* accuracy with largescale molecular dynamics using recently-developed hybrid atomistic-continuum approach, known as twotemperature model coupled deep potential molecular dynamics (TTM-DPMD) [12]. By simulating free-standing

^{*} ddkang@nudt.edu.cn

[†] jydai@nudt.edu.cn

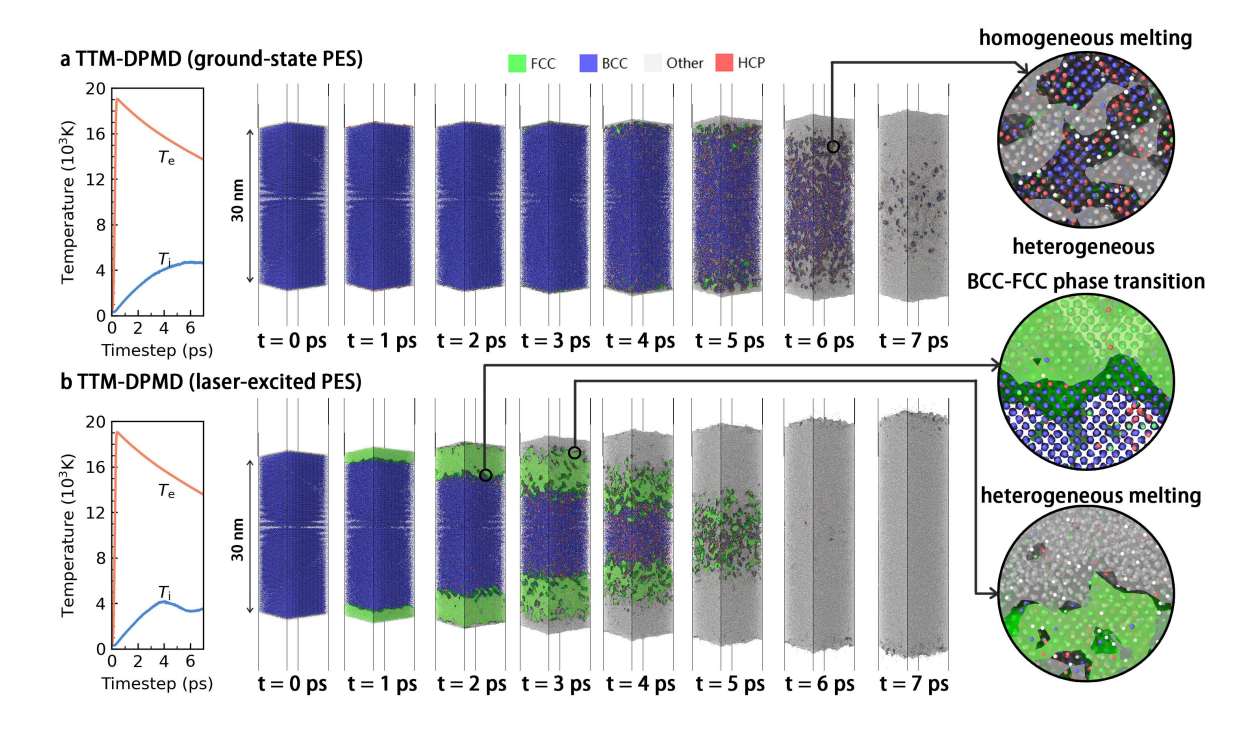


Figure 1. Diverging melting dynamics in laser-excited tungsten. Under absorbed laser fluence of 120 mJ cm⁻², (a) Conventional TTM-MD prediction with groud-state PES $A(\mathcal{R}, T_{\rm i})$ showing homogeneous melting gorvened by electron-phonon coupling. (b) Our ETD-DPMD results with laser-excited PES $A(\mathcal{R}, T_{\rm e})$ revealing electronic pressure-driven heterogeneous melting. The local structures are identified by the polyhedral template matching (PTM) method [25], and polyhedral surface meshes around FCC-type (green) and amorphous-type (gray) particles are constructed to highlight the heterogeneity in lattice symmetry.

tungsten (W) and gold (Au) nanofilms, we uncover the crucial role of electronic pressures in triggering heterogeneous structural transformations at picosecond scales. Time-resolved X-ray diffraction signatures further distinguish this mechanism from thermal expansion, offering experimental validation pathways.

II. RESULTS

Ab initio modeling of laser-driven dynamics. Within the TTM-DPMD framework, the electron temperature dependent deep neural network (ETD-NN) is implemented to capture the ab initio laser-excited PES while maintaining computational efficiency. With ETD-NN, the nonthermal contribution to total energy, forces, and pressure at elevated eletronic temperature $T_{\rm e}$ is inherently incorporated [26]. To ensure the accuracy of our neural network model, we have validated the thermophysical and vibrational properties of W and Au under both equilibrium $(T_e = T_i)$ and non-equilibrium conditions $(T_e \neq T_i)$ [12, 26]. Especially, we reproduced the phonon softening in W along the H-N and $N-\Gamma$ paths in the first Brillouin zone at elevated electron temperatures up to 20,000 K, consistent with previous predictions [27] (see Fig.S1). Under more severe

non-equilibrium state ($T_{\rm e}=22,000~{\rm K}$), an imaginary phonon mode at the N-point was observed, indicating a possible solid-solid phase transition. Here we mainly focus on the moderate non-equilibrium condition below the $T_{\rm e}=20,000~{\rm K}$ to exclude the influence of lattice-instability-driven nonthermal phase transition.

The efficiency of TTM-DPMD approaches enables a full-scale ab initio description where the geometry of the sample is compatible with the experimental conditions. Here, we choose 30-nm-thick W nanofilm [28] and 35-nmthick Au nanofilm [18] as the target sample. Since the foil thickness is comparable to the mean free path of excited electrons (~ 33 nm in W and ~ 100 nm in Au), the ballistic electron transport and reflux inside the foil produces uniform laser energy deposition [29]. Extra vacuum space perpendicular to the laser incident direction (z-axis) is set to allow free surface response to the relaxation of internal stress (including both electronic and thermoelastic contributions). Periodic boundary conditions are applied in the lateral directions to simulate the experimental conditions where laser spot diameter is large (hundreds of microns) compared to the depth of laser energy deposition [30]. More details about TTM-DPMD simulation are provided in the Method Section.

Ultrafast heterogeneous melting dynamics. Here we present structural transformation of laser-

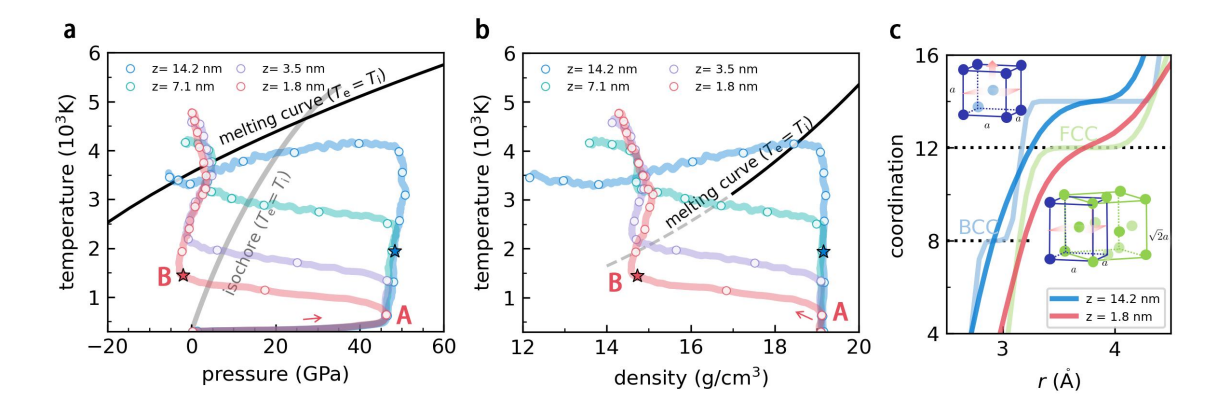


Figure 2. Extreme heterogeneity in laser-excited W. (a)(b) Depth-dependent thermodynamic pathway in the tungsten nanofilm. The absorbed laser fluence is 120 mJ cm⁻² and thermodynamic states are shown by colored circles every 0.5 ps. The melting curve (black solid line) under equilibrium condition ($T_e = T_i$) is obtained via two-phase method [12]. State A marks the initial buildup of electronic pressure (t = 0.5 ps), and state B marks the complete release of electronic pressure (t = 1.5 ps). (c) coordination number of selected region at t = 1.5 ps (as highlighted by colored stars in the Fig.2a,b), which is obtained by integration of radial distribution function. For comparison, a typical coordination of BCC and FCC lattice is presented.

excited W subjected to an absorbed laser fluence of $120 \text{ mJ} \text{ cm}^{-2}$ (duration of laser pulse set to 130 fs). This fluence, although insufficient to trigger dynamical instability in the BCC lattice, reveals significant alterations in melting behavior due to the presence of hot electrons.

For comparison, we firstly discuss the purely thermal process obtained from a traditional TTM-MD method with ground-state PES that does not incorporate laser-modulation (Fig.1a). After laser energy deposition, the system reaches maximum electron temperature $T_{\rm e}=19,050~{\rm K}$ while the lattice remains cold ($T_{\rm i}=300~{\rm K}$). The lattice temperature quickly increases due to electron-phonon energy exchange. Once lattice temperature exceeds the limit of lattice thermal stability, the nucleation of liquid region inside the foil is triggered, known as homogeneous melting mechanism [21]. Within the first 5 ps, surface expansion remains limited to moderate volumetric change (Fig.S2a), as constrained by the timescale of thermal pressure buildup.

The introduction of laser modulation in PES through our ETD-NN model fundamentally alters this picture. As presented in Fig.1b, the W nanofilm quickly responds to laser heating on a sub-picosecond timescale, and exhibits instant surface expansion not observed in a purely thermal process. The heterogeneous nucleation of FCC phase is initially formed in the surface region, then the BCC-FCC transformation front moves inward with an average velocity of $\sim 2571~\rm m~s^{-1}$. Subsequently, as ion temperature increases above $\sim 2200~\rm K$ at $t=2~\rm ps$, although the temperature is significantly lower than the melting point ($T_{\rm m} = 3540 \text{ K}$) under ambient condition, the collapse of crystal structure occurs in the surface region and proceeds inward as the BCC-FCC interface propagates. Such a melting process exhibits a well-defined solid-liquid interface moving inward, which is similar to the heterogeneous melting mechanism but has a high propagation

speed up to $\sim 2500~{\rm m~s^{-1}}$. Here we name this melting behavior as "ultrafast heterogeneous melting" because the melting speed is an order of magnitude greater than that of conventional heterogeneous melting process ($\sim 10^2~{\rm m~s^{-1}}$) [18]. After $t=4~{\rm ps}$, the melt front rapidly advances, completing the melting process within the following two picoseconds.

Electronic pressure-induced thermodynamic and structural heterogeneity. The ultrafast heterogeneous melting process exhibits spatial characteristics akin to conventional heterogeneous melting, with a well-defined melt front, while temporally resembling homogeneous melting due to its rapid progression. Such a unique combination of spatial and temporal features motivates a deeper exploration of the thermodynamic pathways and microscopic mechanisms involved.

As shown in Fig.2a, the ultrafast heating of electrons results in the buildup of extreme internal stress in a subpicosecond timescales. The thermalized electrons with extremely high kinetic energy can contribute to an extra stress of ~ 45 GPa, which is significantly larger than that from thermal atomic vibrations of lattice. With the existence of free surface, a super-high expansion velocity of $\sim 755~\mathrm{m~s^{-1}}$ at the initial state (t = 0.4 ps) is observed (see Fig.S3), and the uniaxial expansion process launches instantly to release this hot-electron-contributed pressure. As shown in Fig.2b, the density in the surface region (z = 1.8 nm) quickly decreases while the interior region (z = 14.2 nm) is heated under the confinement of internal stress. As a consequence, the inhomogeneous thermodynamic profiles are created. In density profile, a well-defined interface with sharp decrease of $\Delta \rho \sim 5 \text{ g cm}^{-3}$ follows the release of stress (see Fig.S2b). This reduced density strongly influences the thermal stability of lattice and explains the early onset of surface disordering below equilibrium melting point.

From a microscopic perspective, the relaxation of electronic stress waves induces local structural transformations. The uniaxial expansion increases interatomic distances perpendicular to the free surface, leading to a transformation from a distorted BCC structure to an FCC structure along the uniaxial Bain deformation path [31]. This observation is similar to the BCC-FCC transition observed by Murphy et al. using isotropic isobaric ab initio MD [32], highlighting the unique role of electronic pressure in modifying phase transitions. As shown in Fig.2c, the short-range order in the laser-excited nanofilm confirms the coexistence of high-density BCC and lowdensity FCC structures. At t = 1.5 ps, the interior atoms display characteristics of a thermally-fluctuated BCC structure, while the surface atoms present typical FCC close-packed structures. This depth-variation in lattice coordination suggests that the density discontinuity driven by electronic pressure is accompanied by a disruption in local lattice symmetry. As the temperature continues to rise, the interplay between lattice heating and electronic pressure relaxation creates a multi-phase system composed of high-density BCC, low-density FCC, and disordered structures.

III. DISCUSSIONS

Laser fluence dependence of structural transformation. To comprehensively understand the lattice response driven by electronic pressure, we performed molecular dynamics simulations under uniaxial isobaricisothermal ensemble ($T_{\rm i}=300~{\rm K},~{\rm p}=1~{\rm bar}$) across a wide range of $T_{\rm e}$ from 10,000 K to 20,000 K.

The equilibrated density and lattice structure is shown in Fig.3a. The structural transformation dynamics exhibits obvious dependence on laser fluence. Under relatively moderate two-temperature state ($T_e \leq 13,000 \text{ K}$), the BCC structure maintains with slight uniaxial distortion. The density decreases from initial value of $19.15 \text{ g cm}^{-3} \text{ to } 17.15 \text{ g cm}^{-3} \text{ at } T_{\rm e} = 13,000 \text{ K, with a}$ uniaxial strain of $\sim 8.81\%$. As the T_e increases, the electronic pressure drives the initial BCC structure towards the more close-packed structure, accompanied with shuffling of several close-packed atomic planes, thus obtaining FCC structure with stacking faults. When the $T_{\rm e}$ exceeds 16,000 K, the stacking faults disappear and pure FCC structure is generated with a density of 14.13 g cm^{-3} at $T_{\rm e} = 20,000$ K, where the corresponding uniaxial strain is as high as 35.43%. A series of TTM-DPMD simulations under different laser fluence confirmed the BCC-FCC phase transition threshold (Fig.S5), once the laser fluence exceeds 80 mJ cm⁻², corresponding to a maximum electron temperature of 15,000 K, the heterogeneous nucleation and growth of FCC structure begin to appear as the uniaxial expansion proceeds.

Further, we investigate the laser fluence dependence of melting mechanism. By calculating the ultrafast electron diffraction pattern, we determine the complete melting

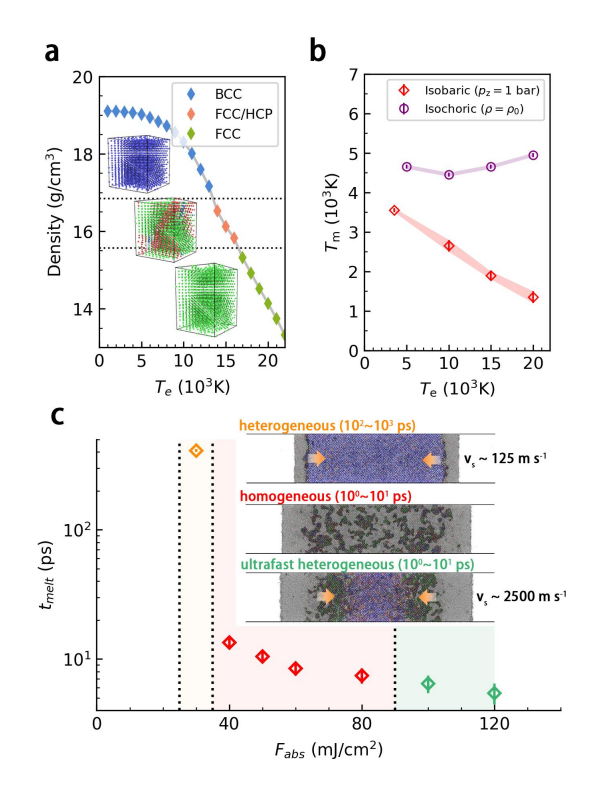


Figure 3. Laser fluence dependence of structural transformation in W. (a) density decrease after electronic pressure relaxation along (100) direction, insets denote the uniaxially-distorted BCC, FCC with stacking faults, and FCC respectively. (b) isochoric and isobaric melting behavior under non-equilibrium condition, obtained from constant- $T_{\rm e}$ DPMD simulations via two-phase method. (c) complete melting time under different laser fluence. The yellow, red, and green region denotes the heterogeneous, homogeneous, and the ultrafast heterogeneous melting mechanism respectively.

time through the decay of (110) diffraction peak during laser heating processes (Fig.S6). For comparison, the results from purely thermal simulation are discussed (Fig.S7). As the laser fluence increases near the melting threshold (53 mJ cm $^{-2}$), the thermal heterogeneous melting starts from the free surface and proceeds slowly by the subsonic melt-front propagation ($\sim 125~{\rm m~s^{-1}}$), such process lasts hundreds of picoseconds. At high laser fluence, the homogeneous melting dominates, where the nucleation and growth of liquid region inside the foil quickly completes the melting within several picoseconds.

When incorporating the laser-excited PES through our ETD-NN model, the threshold fluences to the different melting regimes are reduced, both heterogeneous and homogeneous melting are predicted to occur more rapidly. Moreover, as shown in the Fig.3b, the release of electronic pressure introduces sharp decrease of local density, resulting in significantly reduced melting point in surface region as compared with isochoric condition. Therefore, as ion temperature increases, the low-density surface crystalline can quickly collapse into disordered structure

before the interior melting. Based on TTM-DPMD simulations (Fig.S5), here we can specify the laser fluence needed for triggering the newly discovered "ultrafast heterogeneous melting" process in the Fig.3c. As the initial electron temperature exceeds $T_{\rm e}=16,000$ K, the isobaric melting point can deviate as large as $\Delta T_{\rm m}\sim 2750$ K from isochoric one. Under such condition, the ultrafast heterogeneous process dominates the melting dynamics.

Nonthermal expansion signatures in X-ray diffraction lineouts. To elucidate the unique expansion dynamics under electronic pressure, we analyze the static structure factor S(q), which directly correlates with X-ray diffraction (XRD) measurements. During the laser heating process, internal stress is released at the surface, generating stress waves that propagate inward. This results in a mixed signal representing both the expanded surface region and the isochoric interior region, as captured by S(q).

As shown in Fig.4, we take laser-excited W with laser fluence of $F_{abs}=80~{\rm mJ/cm^2}$ as an example. In the purely thermal process, the dominant role of electron-phonon coupling leads to the accumulation of thermal kinetic pressure inside the foil, thus driving gradual surface expansion. From Fig.4a, the new characteristic peaks splits from the original peak at $q=2.8~{\rm \AA}^{-1}$, then continuously shifts to lower q values, corresponding to the gradual increase in interatomic distance of surface region under uniaxial expansion.

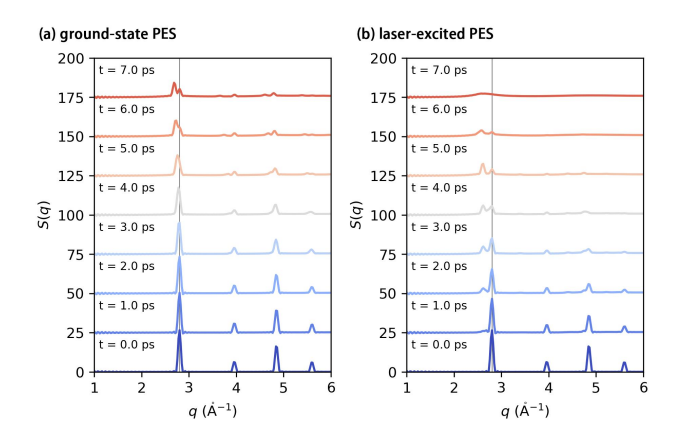


Figure 4. Static structure factor S(q) of laser-excited W nanofilm under laser fluence of 80 mJ/cm², estimated from TTD-DPMD trajectories with (a) ground-state PES (b) laser-excited PES. The black line highlights the first diffraction peak from initial BCC structure.

In nonthermal processes (Fig.4b), the generation of electronic pressure originates from the formation of the initial two-temperature state. Consequently, the release of hot-electron-contributed pressure occurs at subpicosecond timescales, resulting in significant uniaxial distortion. At t=2 ps, the proportion of low-density surface region reaches a detectable level for XRD, resulting in a notable splitting of the first diffraction peak. A new characteristic peak has been observed at $q_{\rm s}=2.613~{\rm \AA}^{-1}$.

Unlike thermal processes, the position of this new peak $q_{\rm s}$ remains unchanged over time. Only its intensity gradually increases, indicating the ongoing nonthermal expansion process. As the lattice temperature increases, the long-range structure of the lattice progressively dissipates, leading to the disappearance of characteristic peaks associated with crystalline structure in S(q) at t=7 ps.

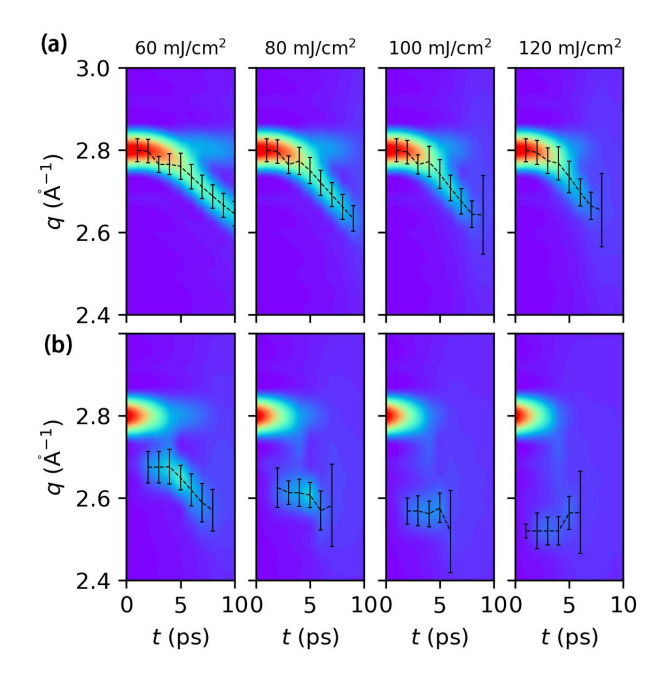


Figure 5. Temporal evolution of static structure factor S(q) of laser-excited W nanofilm at different laser fluence, estimated from TTD-DPMD trajectories with (a) ground-state PES (b) laser-excited PES. The positions of new diffraction peak are marked by black dashed line to highlight the difference between thermal and nonthermal expansion dynamics.

As shown in Fig.5, we present the temporal evolution of S(q) under various laser fluence, ranging from 60 mJ/cm² to 120 mJ/cm², aiming to provide a comprehensive understanding of expansion dynamics. Analysis of the $2.4 - 3.0 \text{ Å}^{-1}$ diffraction regime reveals distinct fluence-dependent behaviors: (1) During thermal expansion, it manifests as continuous shifting, where a higher lattice heating rate can result in a slightly faster shift of the new diffraction peak, as shown in Fig. 5a. (2) During nonthermal expansion process, it exhibits as discontinuous splitting, and the position of the new diffraction peak displays a strong dependence on laser fluence. A larger electron pressure corresponds to a lower q value position of the new peak, as illustrated in Fig.5b. The observed qualitative disparity in expansion dynamics, as indicated by S(q), implies the possibility of identifying evidence of electronic pressure relaxation dynamics through timeresolved X-ray diffraction experimental methodologies.

Ubiquity of heterogeneous structural dynamics. To demonstrate the ubiquity of electronic pressure

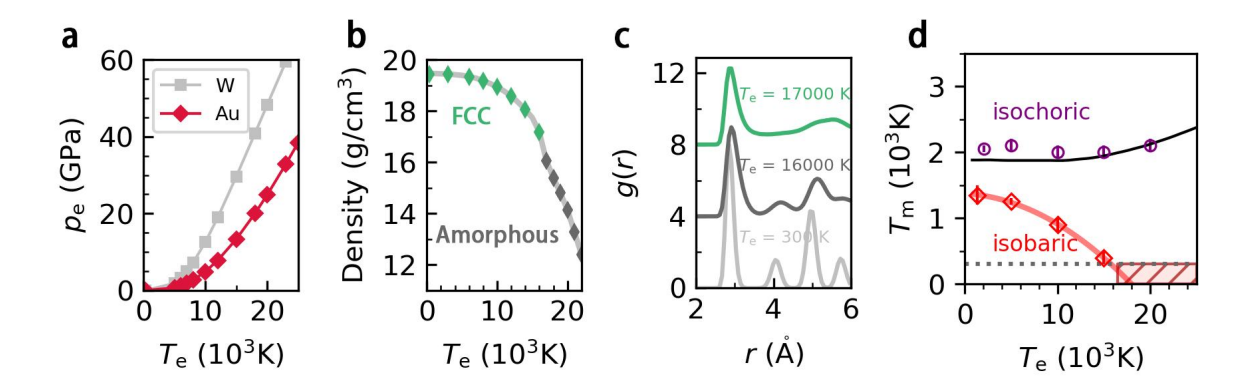


Figure 6. Nonthermal behavior of laser-excited gold. (a) electronic pressure contributed by hot electrons. (b) density decrease and (c) short-range order of laser-excited gold under uniaxial isobaric ensemble (d) isobaric and isochoric melting behavior of laser-excited gold, the black solid line denotes previous lattice dynamics prediction by Smirnov *et al.* [6], and the nonthermal melting regime ($T_{\rm m} \leq 300~{\rm K}$) is filled with red diagonals..

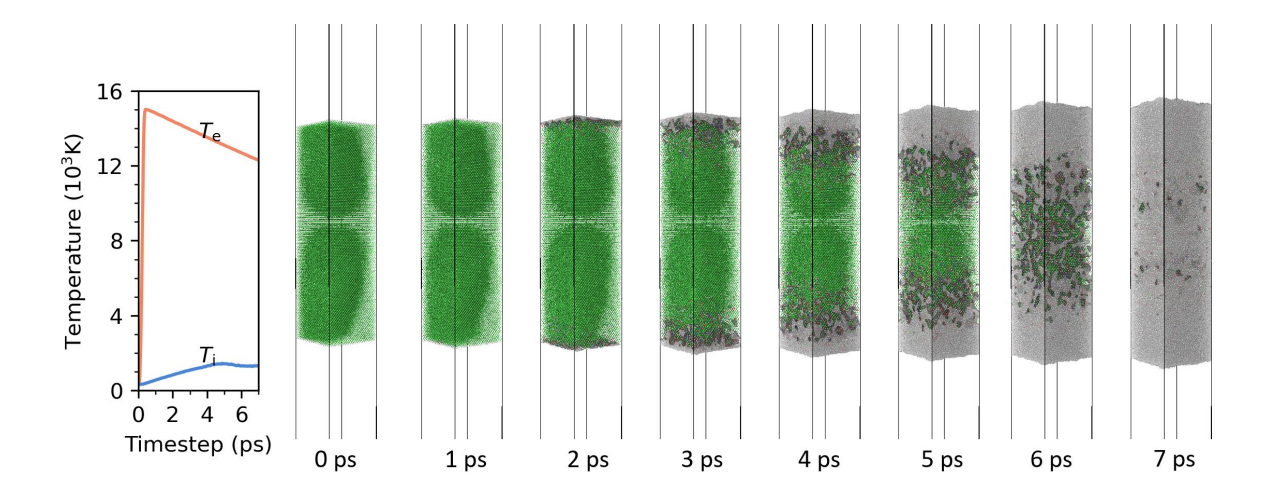


Figure 7. Atomic configurations of laser-heated 35-nm-thick Au nanofilm under laser energy density of 0.80 MJ/kg, where the local symmetry of atoms is identified via PTM method. The green and grey color denotes FCC and disordered structure respectively.

in laser-driven processes, we extend the TTM-DPMD framework to gold (Au), a noble metal with fully occupied d-orbitals. Despite its distinct electronic structure, Au exhibits analogous nonthermal dynamics.

At elevated electron temperatures, the hot electrons also contribute non-negligible electronic pressure in Au (Fig.6a), reaching 25 GPa at $T_{\rm e}=20,000$ K. Under isobaric-isothermal condition ($T_{\rm i}=300$ K, $p_{\rm z}=1$ bar), electronic pressure-induced uniaxial expansion reduces FCC symmetry to face-centered tetragonal (FCT), with corresponding decrease in density from 19.44 g cm⁻³ at $T_{\rm e}=300$ K to 17.17 g cm⁻³ at $T_{\rm e}=16,000$ K (Fig.6bc). As $T_{\rm e}$ reaches 17,000 K, the expansion can even destabilize the lattice, triggering a disordered transition at room temperature ($T_{\rm i}=300$ K)—a "nonthermal melting" regime where amorphization occurs without lattice

heating (Fig.6d). These findings align with the conclusions of Daraszewicz *et al.*, and Medvedev *et al.* regarding nonthermal behaviors under isobaric constraints [13, 14], suggesting that the ultrafast disordering of laser-excited Au is primarily due to electron pressure relaxation process.

Further, large-scale simulations of 35-nm-thick free-standing Au nanofilm (containing 137,600 atoms) confirm ultrafast heterogeneous melting, mirroring W's behavior. As shown in Fig.7, when the laser energy density is set to 0.80 MJ kg $^{-1}$, the initial maximum electron temperature is approximately $\sim 15,000$ K, yielding an electronic pressure contribution of ~ 20 GPa. With the release of electronic pressure, the surface atoms directly transforms into a disordered structure due to significant reduction in melting point. The melt front then moves

inward at a speed of 2,916 m s⁻¹, completing the melting process within 8 ps. These results, along with previous prediction on the widespread existence of electronic pressure in laser-excited materials [11], underscore the pervasive nature of electron pressure relaxation dynamics and ultrafast heterogeneous structural transformation in laser-driven processes.

Summary. By investigating real-time response of laser-excited W and Au nanofilm via TTM-DPMD approach, we unraveled the vital role of the electronic pressure in the laser-driven dynamics, which was previously not fully understood. As an integral part of nonthermal behavior, the electronic pressure builds up simultaneously with appearance of the two-temperature state, wherein the lattice remains cold. At elevated electron temperatures, the additional pressure contributed by hot electrons becomes significant, reaching up to $p_{\rm e} \sim 10^1$ GPa at $T_{\rm e} \sim 10^4$ K. The release of electronic pressure triggers violent uniaxial expansion from free surface, which exhibits a drastic difference from thermal expansion in temporal behaviors, which can be identified by time-resolved X-ray diffraction techniques. As a result, pressure, density, and temperature discontinuity in thermodynamic profile is generated and moves inward at a high speed on the order of 10^3 m s⁻¹.

The following structural transformation is therefore dominated by the relaxation of electronic pressure. Two unexpected phenomena, absent in either purely thermal process or previous lattice dynamics calculations, were observed: (i) heterogeneous solid-solid transition (in W), which directly arises from the expansion process that drives the BCC-FCC transition along the uniaxial Bain path. (ii) ultrafast heterogeneous melting (both in W and Au), which is a combination of density decrease driven by nonthermal expansion and temperature increase induced by electron-phonon coupling. These findings suggest a extreme structural heterogeneity in laser-excited metal, which has a profound influence on the interpretation of experiments and our comprehension of nonthermal behavior.

We also note that this structural transformation is fundamentally different from the conventional nonthermal phase transition driven by lattice instability. The latter is expected to occur in less than a phonon period [8, 33, 34], which can be considered as homogeneous and ultrafast. Instead, the nonthermal expansion induces heterogeneous structural transformation, which can strongly rely on the crystal symmetry, the orientation of free surface, and the strength of nonthermal pressure. Especially, even when phonon spectra suggest a dynamically stable structure, this structural transformation can occur. This is particularly evident in laser-excited Au.

Moreover, considering the interplay between this heterogeneous phase transition and ultrafast melting, whether the intermediate solid phase can be observed by experimental measurements depends on accurate determination of electron-phonon coupling. Especially for the extremely inhomogeneous thermodynamic profile, both

electron temperature and density dependence of electronphonon energy exchange rate should be considered in the future work. On this issue, TTM-DPMD approach can to be coupled with the newly-developed deep learning scheme to infer electronic structure on-the-fly [35].

IV. METHODS

Electron temperature dependent neural network model. To capture the modulation on PES introduced by hot electrons, here we adopt the deep neural network with an additional parameter, electron temperature T_e , named as electron-temperature-dependent deep potential (ETD-DP) model [12],

$$A = A(\mathcal{R}, T_e) = \sum_{i} \mathcal{N}_{\alpha_i}(\mathcal{D}_{\alpha_i}(r_i, \{r_j\}_{j \in n(i)}), T_e)$$
 (1)

where $A(\mathcal{R}, T_e)$ indicates that the free energy depends on the local atomic environment \mathcal{R} and electron temperature, \mathcal{N}_{α_i} denotes the neural network of specified chemical species of α_i of atom i, and the descriptors \mathcal{D}_{α_i} describes the local environment of atom i with its neighbor list $n(i) = \{j | r_{ji} < r_{cut}\}$. The ETD-DP model can inherently incorporate the nonthermal characteristics of laser-excited matters in molecular dynamics simulations, including the hot-electron-modulated atomic forces and virial tensor,

$$\mathbf{F} = -\frac{\partial A}{\partial \mathbf{R}_i} = -\frac{\partial U}{\partial \mathbf{R}_i} + T_e \frac{\partial S}{\partial \mathbf{R}_i}$$
 (2)

$$\mathbf{\Xi} = \frac{\partial A}{\partial \mathbf{\Omega}} \cdot \mathbf{\Omega}^T = \frac{\partial U}{\partial \mathbf{\Omega}} \cdot \mathbf{\Omega}^T - T_e \frac{\partial S}{\partial \mathbf{\Omega}} \cdot \mathbf{\Omega}^T \tag{3}$$

here \mathbf{R}_i denotes the coordinate vector of atom i, Ω denotes a 3×3 matrix formed by three lattice vectors and Ω^T is its transpose. Consider a system composed of N atoms, the total pressure of this electron-ion system is determined by the summation of ionic thermal kinetic contribution and virial contribution.

In the maintext, the ETD-DP model of tungsten is generated with DeePMD-kit packages [36] and DP-Generator [37]. The configurations space with different electronic occupation considered in this work is efficiently sampled. Based on the training data set generated in previous work [12], we further improved the uniaxial expansion behavior of laser-excited tungsten along (100), (110) and (111) direction by sampling additional 1,860 configurations, where the ion temperature ranges from 100 K to 4,000 K, electron temperature ranges from 100 K to 25,000 K.

The details in DP training and Kohm-Sham density functional theory (KS-DFT) calculation is the same as previous work, where the self-consistency calculations are all performed with the VASP packages [38]. The Perdew-Bruke-Erzerhof (PBE) exchange correlation functional is used [39] and psudopotential takes the projector augmented-wave (PAW) formalism [40]. The sam-

pling of Brillouin zone is chosen as 0.2 Å^{-1} under ambient condition and 0.5 Å^{-1} for high temperature ($T \ge 1600 \text{ K}$).

Two-temperature model coupled neural network molecular dynamics approach. To simulate the real-time response of material upon laser excitation, the additional description on electron subsystem is introduced and strongly coupled with atomic system in TTM-DPMD approach. The heat conduction equation of electron continuum characterizes the temporal evolution of electron occupation, thus governing the transition of atomic system between different T_e -dependent PES. Langevin dynamics is incorporated to mimic the dynamic electron-ion collision, thus including the non-adiabatic energy exchange between electron and atomic subsystem,

$$C_e(T_e)\frac{\partial T_e}{\partial t} = \nabla \cdot (\kappa_e \nabla T_e) - g_{ei}(T_e)(T_e - T_i) + S(\mathbf{r}, t)$$
(4

$$m_i \frac{d^2 \mathbf{r}_i}{dt^2} = -\nabla_i A(T_e) - \gamma_i \mathbf{v}_i + \tilde{\mathbf{F}}_i(t)$$
 (5)

where C_e the electron heat capacity, κ_e the electronic thermal conductivity, g_{ei} the electron-phonon coupling constant, $S(\mathbf{r},t)$ the laser source, γ_i the friction parameter, $\tilde{\mathbf{F}}_i$ the random force with Gaussian distribution.

To simulate the material response that relevant to real experimental conditions, here the 30-nm-thick W nanofilm [28] and 35-nm-thick Au nanofilm [18] are chosen as the target sample. A Gaussian temporal profile of laser pulse is used, and the duration is set to 130 fs. Since both the thickness of W and Au nanofilm is comparable to the mean free path of excited electrons (\sim 33 nm in W and \sim 100 nm in Au), the ballistic motion of the excited electrons leads to the fast (within \sim 100 fs) redistribution of the deposited energy within the ballistic range. As a result, the uniform laser energy deposition is expected,

$$S(t) = \frac{F_{\text{abs}}}{\sigma d\sqrt{2\pi}} \exp(-\frac{(t - t_0)^2}{2\sigma^2})$$
 (6)

where $F_{\rm abs}$ the absorbed laser fluence, σ the standard deviation of the temporal Gaussian distribution, d the thickness of nanofilm, t_0 the time zero defined as the arrival of the maximum of the laser pulse. The absorbed laser energy density ϵ can be estimated via $\epsilon = F_{abs}/\rho d$, where ρ the mass density.

In the maintext, the TTM-DPMD simulations is performed with LAMMPS packages [41] through modified EXTRA-FIX module. The electronic heat capacity is obtained by individual DFT calculations $C_e = T_e \frac{\partial S_e}{\partial T_e}$. The electron-phonon coupling is set to constant value of 2.0×10^{17} W m⁻² K⁻¹, and the duration of laser pulse is set to 130 fs. The electron thermal conductivity is described by the Drude model relationship, $\kappa_e(T_e,T_i)=\frac{1}{3}v_F^2C_e(T_e)\tau_e(T_e,T_i)$, where v_F is Fermi velocity and $\tau_e(T_e,T_i)$ is the total electron scattering time defined by the electron-electron and electron-phonon scattering rates, $1/\tau_e=1/\tau_{e-e}+1/\tau_{e-ph}=AT_e^2+BT_i$. The coefficients $A=2.11\times 10^{-4}$ K⁻² ps⁻¹, B=8.4 × 10^{-2} K⁻¹ ps⁻¹, $v_F=9710$ Å ps⁻¹ are adopted.

For atomic system, the sample geometry of 30-nm-thick 100-oriented single-crystalline W foil is a parallelepiped $L_x \times L_y \times L_z$ with $L_x = L_y = 30a_0$ and $L_z = 95a_0$ (171,000 atoms). $a_0 = 3.17104$ Å is the parameter of the elementary BCC cell for W corresponding to the ETD-DP model at 300 K and 0 GPa. Extra 30 nm vacuum space along the z-axis is set to mimic the free boundary condition. Periodic boundary conditions are applied in the lateral directions (x and y-axis). These conditions simulate the experimental situation in which the laser spot diameter is large (hundreds of microns) compared to the depth of the laser energy deposition (tens of nanometers) so that the effects of the edges of the laser beam can be neglected.

M. Guan, D. Chen, S. Hu, H. Zhao, P. You, and S. Meng, Theoretical insights into ultrafast dynamics in quantum materials, Ultrafast Science 2022, 1 (2022).

^[2] E. M. Rafael R. Gattass, Femtosecond laser micromachining in transparent materials, Nat. Photonics 2, 219 (2008).

^[3] D. M. Fritz, D. A. Reis, B. Adams, R. A. Akre, J. Arthur, C. Blome, P. H. Bucksbaum, A. L. Cavalieri, S. Engemann, S. Fahy, R. W. Falcone, P. H. Fuoss, K. J. Gaffney, M. J. George, J. Hajdu, M. P. Hertlein, P. B. Hillyard, M. H. von Hoegen, M. Kammler, J. Kaspar, R. Kienberger, P. Krejcik, S. H. Lee, A. M. Lindenberg, B. McFarland, D. Meyer, T. Montagne, E. D. Murray, A. J. Nelson, M. Nicoul, R. Pahl, J. Rudati, H. Schlarb,

D. P. Siddons, K. Sokolowski-Tinten, T. Tschentscher, D. von der Linde, and J. B. Hastings, Ultrafast bond softening in bismuth: Mapping a solid interatomic potential with x-rays, Science **315**, 633 (2007).

^[4] W. Liu, J. Luo, S. Li, and L. Wang, The seeds and homogeneous nucleation of photoinduced nonthermal melting in semiconductors due to self-amplified local dynamic instability, Sci. Adv. 8, eabn4430 (2022).

^[5] V. Recoules, J. Clerouin, G. Zerah, P. M. Anglade, and S. Mazevet, Effect of intense laser irradiation on the lattice stability of semiconductors and metals, Phys. Rev. Lett. 96, 055503 (2006).

^[6] N. A. Smirnov, Copper, gold, and platinum under femtosecond irradiation: Results of first-principles calcula-

- tions, Phys. Rev. B 101, 094103 (2020).
- [7] B. Arnaud and Y. Giret, Electron cooling and debyewaller effect in photoexcited bismuth, Phys Rev Lett 110, 016405 (2013).
- [8] E. S. Zijlstra, J. Walkenhorst, and M. E. Garcia, Anharmonic noninertial lattice dynamics during ultrafast nonthermal melting of insb, Phys Rev Lett 101, 135701 (2008).
- [9] C. Lian, S. B. Zhang, and S. Meng, Ab initio evidence for nonthermal characteristics in ultrafast laser melting, Phys. Rev. B 94, 184310 (2016).
- [10] S. Khakshouri, D. Alfè, and D. M. Duffy, Development of an electron-temperature-dependent interatomic potential for molecular dynamics simulation of tungsten under electronic excitation, Phys. Rev. B 78, 224304 (2008).
- [11] E. Bévillon, J. P. Colombier, V. Recoules, and R. Stoian, Free-electron properties of metals under ultrafast laser-induced electron-phonon nonequilibrium: A first-principles study, Phys. Rev. B 89, 115117 (2014).
- [12] Q. Zeng, B. Chen, S. Zhang, D. Kang, H. Wang, X. Yu, and J. Dai, Full-scale ab initio simulations of laser-driven atomistic dynamics, npj Comput. Mater. 9, 213 (2023).
- [13] S. L. Daraszewicz, Y. Giret, N. Naruse, Y. Murooka, J. Yang, D. M. Duffy, A. L. Shluger, and K. Tanimura, Structural dynamics of laser-irradiated gold nanofilms, Phys. Rev. B 88, 184101 (2013).
- [14] N. Medvedev and I. Milov, Nonthermal phase transitions in metals, Sci. Rep. 10, 12775 (2020).
- [15] A. Descamps, B. K. Ofori-Okai, O. Bistoni, Z. Chen, E. Cunningham, L. B. Fletcher, N. J. Hartley, J. B. Hastings, D. Khaghani, M. Mo, B. Nagler, V. Recoules, R. Redmer, M. Schrner, D. G. Senesky, P. Sun, H.-E. Tsai, T. G. White, S. H. Glenzer, and E. E. McBride, Evidence for phonon hardening in laser excited gold using x ray diffraction at a hard x- ray free electron laser, Sci. Adv. 10, eadh5272 (2024).
- [16] G. A. de la Pena Munoz, A. A. Correa, S. Yang, O. Delaire, Y. Huang, A. S. Johnson, T. Katayama, V. Krapivin, E. Pastor, D. A. Reis, S. Teitelbaum, L. Vidas, S. Wall, and M. Trigo, Ultrafast lattice disordering can be accelerated by electronic collisional forces, Nat. Phys. 19, 1489 (2023).
- [17] R. Ernstorfer, M. Harb, C. T. Hebeisen, G. Sciaini, T. Dartigalongue, and R. D. Miller, The formation of warm dense matter: experimental evidence for electronic bond hardening in gold, Science 323, 1033 (2009).
- [18] M. Mo, Z. Chen, R. Li, M. Dunning, B. Witte, J. Baldwin, L. Fletcher, J. Kim, A. Ng, R. Redmer, et al., Heterogeneous to homogeneous melting transition visualized with ultrafast electron diffraction, Science 360, 1451 (2018).
- [19] J. M. Molina and T. G. White, A molecular dynamics study of laser-excited gold, Matter Radiat. Extrem. 7, 036901 (2022).
- [20] M. I. Arefev, M. V. Shugaev, and L. V. Zhigilei, Kinetics of laser-induced melting of thin gold film: How slow can it get?, Sci. Adv. 8, eabo2621 (2022).
- [21] D. S. Ivanov and L. V. Zhigilei, Combined atomisticcontinuum modeling of short-pulse laser melting and disintegration of metal films, Phys. Rev. B 68, 064114 (2003).
- [22] Q. Zeng and J. Dai, Structural transition dynamics of the formation of warm dense gold: From an atomic scale view, Sci. China-Phys. Mech. Astron. **63**, 1 (2020).

- [23] S. Lu, L. Xie, K. Lai, R. Chen, L. Cao, K. Hu, X. Wang, J. Han, X. Wan, J. Wan, Q. Dai, F. Song, J. He, J. Dai, J. Chen, Z. Wang, and G. Wang, Plasmonic evolution of atomically size-selected au clusters by electron energy loss spectrum, Natl Sci Rev 8, nwaa282 (2021).
- [24] J. Xu, D. Chen, and S. Meng, Decoupled ultrafast electronic and structural phase transitions in photoexcited monoclinic vojsub¿2j/sub¿, Sci. Adv. 8, eadd2392 (2022).
- [25] P. M. Larsen, S. Schmidt, and J. Schi{o}tz, Robust structural identification via polyhedral template matching, Modelling Simul. Mater. Sci. Eng. 24, 055007 (2016).
- [26] Supplemental material, See Supplemental Material for details about the thermodynamic evolution and structural transformation in TTM-DPMD.
- [27] Y. Giret, S. L. Daraszewicz, D. M. Duffy, A. L. Shluger, and K. Tanimura, Nonthermal solid-to-solid phase transitions in tungsten, Phys. Rev. B 90, 094103 (2014).
- [28] M. Mo, S. Murphy, Z. Chen, P. Fossati, R. Li, Y. Wang, X. Wang, and S. Glenzer, Visualization of ultrafast melting initiated from radiation-driven defects in solids, Sci. Adv. 5, eaaw0392 (2019).
- [29] Z. Chen, V. Sametoglu, Y. Y. Tsui, T. Ao, and A. Ng, Flux-limited nonequilibrium electron energy transport in warm dense gold, Phys Rev Lett 108, 165001 (2012).
- [30] Z. Chen, M. Mo, L. Soulard, V. Recoules, P. Hering, Y. Tsui, S. Glenzer, and A. Ng, Interatomic potential in the nonequilibrium warm dense matter regime, Phys. Rev. Lett. 121, 075002 (2018).
- [31] G. Grimvall, B. Magyari-Köpe, V. Ozolinš, and K. A. Persson, Lattice instabilities in metallic elements, Rev. Mod. Phys. 84, 945 (2012).
- [32] S. T. Murphy, S. L. Daraszewicz, Y. Giret, M. Watkins, A. L. Shluger, K. Tanimura, and D. M. Duffy, Dynamical simulations of an electronically induced solid-solid phase transformation in tungsten, Phys. Rev. B 92, 134110 (2015).
- [33] S. Wall, S. Yang, L. Vidas, M. Chollet, J. M. Glownia, M. Kozina, T. Katayama, T. Henighan, M. Jiang, T. A. Miller, D. A. Reis, L. A. Boatner, O. Delaire, and M. Trigo, Ultrafast disordering ofvanadium dimers in photoexcited vo2, Science 362, 6414 (2018).
- [34] X. Wang, J. C. Ekstrom, A. U. J. Bengtsson, A. Jarnac, A. Jurgilaitis, V. T. Pham, D. Kroon, H. Enquist, and J. Larsson, Role of thermal equilibrium dynamics in atomic motion during nonthermal laser-induced melting, Phys Rev Lett 124, 105701 (2020).
- [35] Q. Zeng, B. Chen, X. Yu, S. Zhang, D. Kang, H. Wang, and J. Dai, Towards large-scale and spatiotemporally resolved diagnosis of electronic density of states by deep learning, Phys. Rev. B 105, 174109 (2022).
- [36] J. Zeng, D. Zhang, D. Lu, P. Mo, Z. Li, Y. Chen, M. Rynik, L. Huang, Z. Li, S. Shi, Y. Wang, H. Ye, P. Tuo, J. Yang, Y. Ding, Y. Li, D. Tisi, Q. Zeng, H. Bao, Y. Xia, J. Huang, K. Muraoka, Y. Wang, J. Chang, F. Yuan, S. L. Bore, C. Cai, Y. Lin, B. Wang, J. Xu, J. X. Zhu, C. Luo, Y. Zhang, R. E. A. Goodall, W. Liang, A. K. Singh, S. Yao, J. Zhang, R. Wentzcovitch, J. Han, J. Liu, W. Jia, D. M. York, W. E, R. Car, L. Zhang, and H. Wang, Deepmd-kit v2: A software package for deep potential models, J. Chem. Phys. 159, 054801 (2023).
- [37] L. Zhang, D.-Y. Lin, H. Wang, R. Car, and E. Weinan, Active learning of uniformly accurate interatomic potentials for materials simulation, Phys. Rev. Materials 3, 023804 (2019).

- [38] G. Kresse and J. Furthmüller, Efficient iterative schemes for ab initio total-energy calculations using a plane-wave basis set, Phys. Rev. B 54, 11169 (1996).
- [39] J. P. Perdew, K. Burke, and M. Ernzerhof, Generalized gradient approximation made simple, Phys. Rev. Lett. 77, 3865 (1996).
- [40] P. E. Blöchl, Projector augmented-wave method, Phys. Rev. B 50, 17953 (1994).
- [41] S. Plimpton, Fast parallel algorithms for short-range molecular dynamics, J. Comput. Phys. 117, 1 (1995).

V. ACKNOWLEDGMENTS

This work was supported by the National Natural Science Foundation of China under Grant Nos. 12304307, 12122103, 12104507, the Science and Technology Innovation Program of Hunan Province under Grant No. 2021RC4026, and Postgraduate Technology Innovation Program of Hunan Province under Grant No.CX20220070.

VI. AUTHOR CONTRIBUTIONS

Q.Z and J. D. proposed the original idea and designed the research. Q. Z. carried out the simulations, Q. Z., X. Y., D. K., and J.D. analyzed and interpreted the results. Q. Z, X. Y. and J. D. wrote the manuscript with the help from other authors. B. C., S. Z., and K. C. provided additional support for the interpretation of the results. All the authors reviewed the manuscript.

VII. COMPETING INTERESTS

The authors declare no competing interests.

VIII. ADDITIONAL INFORMATION

Supplementary information is available for this paper